Inflammation-induced subventricular zone dysfunction leads to olfactory deficits in a targeted mouse model of multiple sclerosis.

Vanja Tepavčević, Françoise Lazarini, Clara Alfaro-Cervello, Christophe Kerninon, Kazuaki Yoshikawa, José Manuel Garcia-Verdugo, Pierre-Marie Lledo, Brahim Nait-Oumesmar, Anne Baron-van Evercooren

Inflammation-induced subventricular zone dysfunction leads to olfactory deficits in a targeted mouse model of multiple sclerosis

Vanja Tepavčević,[1,2,3] Françoise Lazarini,[4,5] Clara Alfaro-Cervello,[6,7] Christophe Kerninon,[1,2,3] Kazuaki Yoshikawa,[8] José Manuel Garcia-Verdugo,[6,7] Pierre-Marie Lledo,[4,5] Brahim Nait-Oumesmar,[1,2,3,9] and Anne Baron-Van Evercooren[1,2,3,9]

[1]UPMC, CRICM, UMR-S 975, Paris, France. [2]INSERM U975, Paris, France. [3]CNRS UMR 7225, Paris, France. [4]Institut Pasteur, Laboratory for Perception and Memory, Department of Neurosciences, Paris, France. [5]CNRS URA2182, Paris, France. [6]Laboratorio de Morfología Celular, Centro de Investigación Príncipe Felipe, CIBERNED, Valencia, Spain. [7]Laboratorio de Neurobiología Comparada, Instituto Cavanilles, Universidad de Valencia, Valencia, Spain. [8]Laboratory of Regulation of Neuronal Development, Institute for Protein Research, Osaka University, Osaka, Japan. [9]AP-HP, Hôpital Pitié-Salpêtrière, Fédération de Neurologie, Paris, France.

Neural stem cells (NSCs) persist in defined brain niches, including the subventricular zone (SVZ), throughout adulthood and generate new neurons destined to support specific neurological functions. Whether brain diseases such as multiple sclerosis (MS) are associated with changes in adult NSCs and whether this might contribute to the development and/or persistence of neurological deficits remains poorly investigated. We examined SVZ function in mice in which we targeted an MS-like pathology to the forebrain. In these mice, which we refer to herein as targeted EAE (tEAE) mice, there was a reduction in the number of neuroblasts compared with control mice. Altered expression of the transcription factors Olig2 and Dlx2 in the tEAE SVZ niche was associated with amplification of pro-oligodendrogenic transit-amplifying cells and decreased neuroblast generation, which resulted in persistent reduction in olfactory bulb neurogenesis. Altered SVZ neurogenesis led to impaired long-term olfactory memory, mimicking the olfactory dysfunction observed in MS patients. Importantly, we also found that neurogenesis was reduced in the SVZ of MS patients compared with controls. Thus, our findings suggest that neuroinflammation induces functional alteration of adult NSCs that may contribute to olfactory dysfunction in MS patients.

Introduction

Neurogenesis by adult neural stem cells (NSCs) persists in defined compartments of the adult CNS (1). The subventricular zone (SVZ) is the largest adult NSC niche. In healthy rodents, SVZ astrocytes (type B cells) proliferate slowly and generate rapidly dividing type C cells, which differentiate into migrating neuroblasts (type A cells) (2). Neuroblasts migrate within the rostral migratory stream (RMS) to the olfactory bulb (OB) and give rise mainly to new interneurons (3) whose main function appears to be constitution/restitution of long-lasting olfactory traces (4, 5). In addition to sustaining OB neurogenesis, the adult SVZ also constitutively contributes to periventricular oligodendrogenesis, although to a lesser extent (6). SVZ neurogenesis/oligodendrogenesis balance is determined by transcription factor interplay, wherein Dlx2 and Pax6 act as neurogenic determinants and Mash1 and Olig2 promote oligodendrocyte and in some cases astrocyte generation (6–10). In the human brain, neuroblasts are generated in the SVZ (11, 12), and newly formed neurons have been detected in the OB (13). However, the contribution of the SVZ to OB neurogenesis and olfaction in humans is unclear (11, 12).

Multiple sclerosis (MS) is a chronic inflammatory demyelinating CNS disease whose progression is associated with the development of permanent neurological disability (14). Periventricular demyelinating lesions are frequent in MS (15). Analyses of the SVZ areas proximal to such lesions have suggested increased early oligodendrogenesis and emigration of precursors into the parenchyma (16, 17), but the consequences of such pathological events on neurogenic function are unknown. Interestingly, olfactory deficits are common in MS patients (18).

Studies examining the SVZ in animal models of MS have focused mainly on the potential of the niche to generate remyelinating cells. Increased oligodendrogenesis has been systematically observed following non-immune periventricular demyelination (6, 19–21) and in diffuse experimental autoimmune encephalomyelitis (EAE) (22, 23), a model of MS characterized by CNS inflammation and clinical signs. However, the niche integrity during chronic inflammation remains unclear (22, 23) and the SVZ neuronal supply to the OB and olfaction during MS-like pathology uninvestigated.

We aimed to examine whether MS-like pathology affects SVZ constitutive neurogenesis and olfaction. As diffuse myelin oligodendrocyte glycoprotein–induced (MOG-induced) EAE mostly affects the spinal cord and, consequently, demyelination in the SVZ vicinity is rare or minimal, we targeted chronic-type EAE lesions to the corpus callosum. SVZ function was investigated by examining the niche structure, neurogenic/oligodendrogenic transcription factor expression, OB neurogenesis, and olfaction. We found that the pathology induced a functional switch in the niche as it expanded the pro-oligodendrogenic type C cell population at the expense of the SVZ neuronal supply to adult OB circuits, which led to a deficit in long-term olfactory memory. Moreover, analyses of the SVZ from MS brains showed decreased neuroblast density in diseased brains. Importantly, we provide evidence that

Authorship note: Brahim Nait-Oumesmar and Anne Baron-Van Evercooren are co–senior authors.

Conflict of interest: The authors have declared that no conflict of interest exists.

Citation for this article: *J Clin Invest.* 2011;121(12):4722–4734. doi:10.1172/JCI59145.

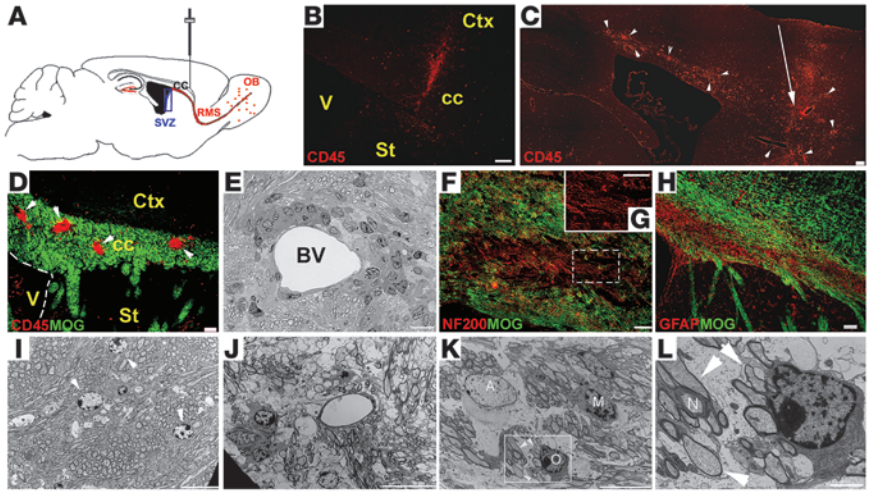

Figure 1

Inflammation and demyelination in the forebrain of tEAE mice. (**A**) Schematic illustration of sagittal mouse brain section indicating cytokine injection site used to achieve tEAE. (**B**) Cytokine injection in non-immunized mice induces restricted infiltration of CD45$^+$ hematopoietic cells to injection site 3 days p.i. (**C**) Cytokine injection into MOG peptide–immunized mice induces widespread CD45$^+$ cell infiltration at the injection site (arrow) and throughout the surrounding cortex and corpus callosum (arrowheads) during the first week p.i. (**D**) Co-immunolabeling for CD45 and MOG reveals inflammatory foci (arrowheads) in tEAE corpus callosum. (**E**) Toluidine blue–stained resin section of tEAE corpus callosum showing inflammatory cells surrounding a blood vessel (BV), 3 days p.i. (**F**) Bundles of demyelinated axons and (**H**) astrocytosis in the demyelinated area 2 weeks p.i. (**G**) Higher-power view of axons within the boxed area shown in **F**. (**I**–**L**) Electron micrographs of corpus callosum. (**I**).Oligodendrocytes (arrowheads) and myelinated axons in control mice. (**J**) Demyelination and axonal swelling in tEAE mice 2 weeks p.i. (**K**) Large astrocyte (A), active microglia (M), thin myelin sheets (arrowheads), and cell with young oligodendrocyte morphology (O) in tEAE tissue, 1 month p.i. (**L**) Higher-power view of the boxed area shown in **K**. Arrows indicate axons surrounded by thin myelin sheets as in **K**, while N labels an axon ensheathed by normal myelin. cc, corpus callosum; Ctx, cortex; St, striatum; V, lateral ventricle. Scale bars: 50 μm (**B**, **D**, and **H**), 100 μm (**C**), 25 μm (**F**), 10 μm (**E, G**, **I**–**K**), 2 μm (**L**).

MS-like pathology induces long-lasting modifications of the SVZ stem cell niche that contribute to olfactory dysfunction.

Results

Inflammation, myelin loss, and axonal pathology during targeted EAE. EAE targeting was achieved by TNF-α/IFN-γ stereotaxic injection into the corpus callosum of mice immunized subclinically with MOG peptide (Figure 1A; see chart in Supplemental Experimental Procedures). These mice are hereafter referred to as targeted EAE (tEAE) mice. Inflammatory lesions were not found in mice immunized subclinically and sacrificed on injection day. In non-immunized (naive) mice, cytokine injection transiently increased CD45$^+$ cell numbers (Supplemental Figure 1A; supplemental material available online with this article; doi:10.1172/JCI59145DS1) only locally, without inducing overall forebrain inflammation (Figure 1B).

Forebrains of tEAE mice sacrificed during the first week post-injection (p.i.) showed prominent inflammation at the injection site within the corpus callosum, but also within surrounding forebrain areas (Figure 1C). The corpus callosum contained numerous dispersed inflammatory foci (Figure 1D) detected mostly in the vicinity of blood vessels (Figure 1E). Quantification of CD45$^+$ cells in the corpus callosum showed a 5-fold increase compared with naive mice injected with cytokines (Supplemental Figure 1A). Most inflammatory cells were F4/80$^+$ macrophages and CD4$^+$ T cells, while CD8$^+$ T cells were present to a minor extent (data not shown). The structures distant to the forebrain contained only occasional inflammatory foci. Mice at this stage showed no signs of limb weakness.

Two weeks p.i, CD45$^+$ cells remained in the corpus callosum, but their numbers decreased 3.7-fold compared with 3 days p.i. (Supplemental Figure 1A). The inflammation was predominantly found in the injection area. Immunohistochemistry (IHC) for MOG, neurofilament-200 (NF-200), and glial fibrillary acidic protein (GFAP) showed the presence of demyelinated axons (Figure 1, F and G) and astrocytosis (Figure 1H). While EM analysis of the control corpus callosum revealed myelinated axons, oligodendrocytes, and absence of inflammation (Figure 1I), myelin loss (Figure 1J) and axonal injury reflected by axonal swelling were observed in tEAE mice 2 weeks p.i. Inflammatory cells persisted in tEAE forebrains 1 and 2 months p.i., albeit to a lesser extent compared with earlier phases (Supplemental Figure 1A). Evidence of both remyelination (Figure 1, K and L) and axonal injury/loss was observed.

SVZ inflammation during tEAE. To examine the effect of tEAE on the SVZ, we first analyzed the dynamics of hematopoietic cells in the neurogenic niche. Control SVZ was generally free of cells strongly stained for CD45 (Figure 2A). While sham (saline) injection did not alter the numbers of SVZ CD45$^+$ cells (data not shown), an 18-fold increase was observed in cytokine-injected naive mice sacrificed 3 days p.i. (Figure 2, B and E). Yet these levels were downregulated during the second week p.i. (data not shown). In tEAE mice sacrificed 3–7 days p.i., numbers of CD45$^+$ cells in the SVZ increased 200- to 250-fold compared with the controls (Figure 2, C and E). Inflammation was also evident in the RMS (Supplemental Figure 1D). Both microglia/macrophages (Supplemental Figure 1, B and C) and T lymphocytes (CD3$^+$, CD4$^+$, or CD8$^+$) were detected. Two months p.i., CD45$^+$ cell numbers in the SVZ decreased compared with early phases but remained 6-fold higher than in the controls (Figure 2, D and E), suggesting sustained inflammation within neurogenic areas of tEAE mice.

SVZ proliferation is modulated in a time-dependent manner during tEAE. We investigated proliferation by subjecting mice to two pulses of BrdU at 2-hour intervals prior to sacrifice. Sham injection did not affect BrdU$^+$ SVZ cell numbers compared with controls (data not shown). However, a transient decrease was observed in tEAE mice 3 days p.i. (Figure 2, F, G, and J), followed by a 3-fold increase in BrdU$^+$ cell numbers at 7 days p.i. (Figure 2, H and J). Two weeks p.i., SVZ proliferation returned to basal levels (data not shown), which remained unchanged at 2 months p.i. (Figure 2, I and J). Similar results were obtained with Ki-67 labeling in a separate experiment (data not shown). Co-immunolabeling for BrdU and cell-specific markers during proliferation peak (7 days)

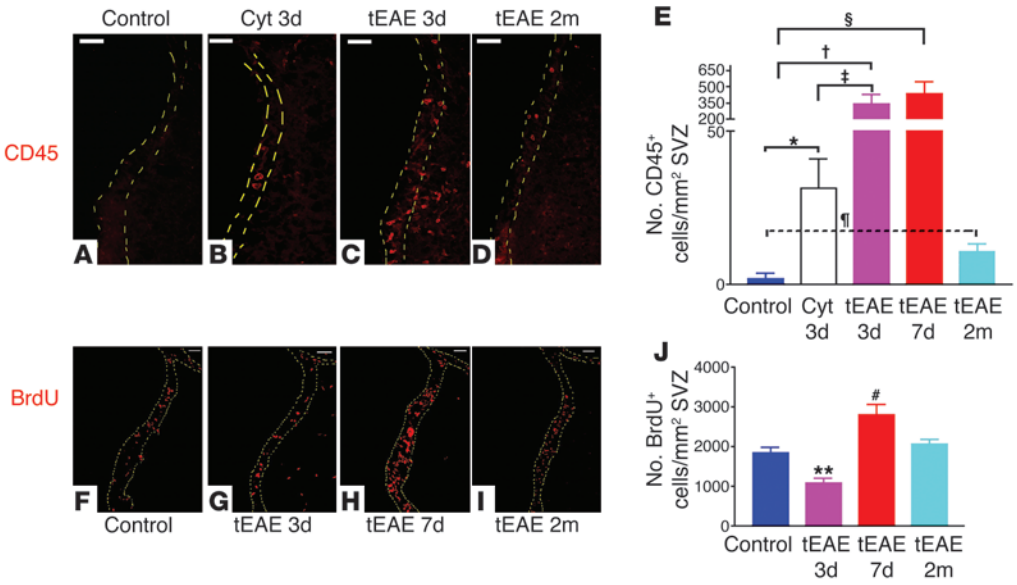

Figure 2

SVZ inflammation correlates with modulation of proliferation in tEAE mice in a time-dependent manner. (**A**–**D**) IHC for CD45 in the SVZ. (**A**) Absence of strongly labeled cells in the SVZ of control mice. (**B**) Cytokine injection into non-immunized mice leads to a moderate increase in hematopoietic cell numbers in the SVZ 3 days p.i. (cyt 3d). (**C**) Extensive increase in numbers of inflammatory cells during the first week p.i. occurs in MOG peptide–immunized mice (tEAE 3d). (**D**) Numbers of inflammatory cells decrease in tEAE mice sacrificed at 2 months p.i. (tEAE 2m) compared with early phases but do not reach control levels. (**E**) Quantification of CD45$^+$ cells in the SVZ (n = 3–4 mice/group; $^*P$ = 0.04, $^\dagger P$ = 0.01, $^\ddagger P$ = 0.02, $^\S P$ = 0.01, $^\P P$ = 0.04). (**F**–**I**) IHC for BrdU in the SVZ. (**F**) Control SVZ. (**G**) Decrease in BrdU$^+$ cell numbers in tEAE SVZ 3 days p.i., while proliferation is upregulated in the neighboring parenchyma. (**H**) Increase in BrdU$^+$ cell numbers in the SVZ at 7 days p.i. (**I**) Recovery of basal levels 2 months p.i. (**J**) Quantification of BrdU$^+$ cells in the SVZ (n = 5–7 mice/group; $^{**}P$ = 0.0026, $^\#P$ = 0.004 versus control). Error bars represent SEM. Scale bars: 50 μm.

showed that 50% of proliferating SVZ cells were Mash1$^+$, 4% were Olig2$^+$, and the remaining ones were GFAP$^+$, except for rare polysialylated neuronal cell adhesion molecule–positive (PSA-NCAM$^+$) and CD45$^+$ cells (less than 1%).

Reduction in SVZ neuroblast numbers during tEAE. To investigate SVZ neurogenesis, we quantified SVZ type A cells using IHC for doublecortin (DCX) or PSA-NCAM. In the SVZ/RMS of control and sham mice, DCX$^+$ and PSA-NCAM$^+$ cells were present along the ventricular wall and RMS (Figure 3, A and F, and Supplemental Figure 2A). In tEAE mice sacrificed during the first week p.i., SVZ immunoreactivity for DCX decreased 3.3-fold (Figure 3, B and E) and that for PSA-NCAM 2.9-fold (Supplemental Figure 2, B and E). DCX$^+$ or PSA-NCAM$^+$ cells were present within small dispersed clumps (Figure 3B and Supplemental Figure 2, B and C). Some of the PSA-NCAM$^+$ cells within the clumps colabeled with cleaved caspase-3 antibody (Supplemental Figure 2F, inset), suggesting ongoing apoptosis. Neuroblast chains were detected outside the SVZ limits, indicating their emigration into the striatum (Figure 3B). At 2 months p.i, regional variability in neuroblast recovery was observed, with large areas containing very few cells (Figure 3C and Supplemental Figure 2D) alternating with cellular bulks, outside which numerous neuroblasts were observed in the striatum (Figure 3D). The average levels of PSA-NCAM and DCX immunoreactivity remained lower than in the controls (DCX, 1.6-fold, Figure 3E; PSA-NCAM, 2.6-fold, Supplemental Figure 2E).

During early pathology phases, altered PSA-NCAM/DCX expression was also evident in the RMS with regional chain reduction (data not shown) alternating with cell accumulation and neuroblasts detected ectopically in the corpus callosum (Figure 3G). By 2 months p.i., chain migration interruptions were evident (Figure 3H). Persistent reduction in migrating neuroblasts did not occur in cytokine-injected naive animals (Figure 3E), as numerous chains were present along the ventricular wall, suggesting that neuroblast loss is caused by tEAE pathology rather than being a direct consequence of TNF-α/IFN-γ injection.

Ultrastructural analysis of the SVZ shows neuroblast loss and type C cell amplification. Next, we analyzed the SVZ ultrastructure in control versus tEAE mice. In control, sham-injected, or immunized non-injected mice, the SVZ was organized as previously described (24). Ependymal multiciliated cells, some astrocytes (type B1) contacting the lateral ventricle through a thin expansion, chains of migrating neuroblasts surrounded by astrocytes (Figure 4A and Supplemental Figure 3A), transit amplifying cells (type C) cells, scarce microglia, and occasional pyknotic cells were present. Striking changes were observed in tEAE mice 3 days p.i., such as thinning of the ependymal layer, decreased B1 cell numbers (Supplemental Table 1), increased numbers of microglia/phagocytic macrophages, and inflamed blood vessels (Figure 4B). Neuroblast numbers decreased (Figure 4, B and E), and remaining chains appeared disrupted (Supplemental Figure 3B). Numbers of pyknotic cells, mostly present within inflamed areas (Figure 4B), slightly increased, unlike those of type C cells (Supplemental Table 1). SVZ of tEAE mice sacrificed 7 days p.i. showed attempts at recovery evidenced by increased total cell numbers (Supplemental Table 1), numerous large astrocytes, and C cells (Figure 4C, lower panel, and Supplemental Figure 3) and somewhat increased chain numbers compared with 3 days p.i. (Figure 4, C and E). Yet these chains were reduced in size (Figure 4C, upper panel) and sometimes detected away from the SVZ, next to striatal vessels

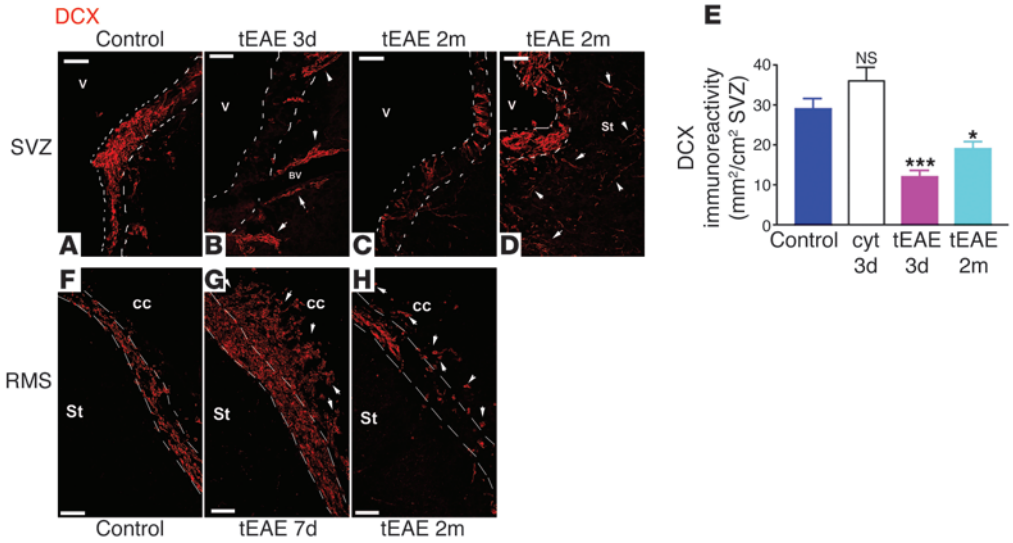

Figure 3

Reduction in neuroblast chains in the tEAE SVZ. (**A**) Numerous DCX$^+$ cells are present in the control subependymal area. (**B**) SVZ areas free of DCX$^+$ cells with chains emigrating into the neighboring striatum (arrowheads) along the blood vessels in tEAE tissue 3 days p.i. (**C** and **D**) SVZ in tEAE mice sacrificed 2 months p.i. (**C**) Areas containing few DCX$^+$ cells alter with those containing bulks of DCX$^+$ cells as shown in **D**. Arrowheads in **D** show individual DCX$^+$ cells in the striatum near the SVZ. SVZ limits are indicated by white dashed lines. (**E**) Quantification of DCX immunoreactivity in the SVZ (n = 3–6 mice/group). Decreases compared with the controls are significant in tEAE mice at 3 days and 2 months p.i. (***P = 0.0002 and **P = 0.0087, respectively), but no significant changes in the amount of DCX were observed in non-immunized mice sacrificed 3 days following cytokine injection as compared with the controls. Error bars represent SEM. (**F**–**H**) RMS in control versus tEAE mice. (**F**) Organized chain migration toward OB in control RMS. (**G**) Accumulation of DCX$^+$ cells within the RMS region proximal to the SVZ and emigration into the corpus callosum at 7 days p.i. (arrowheads). (**H**) Interruptions of the RMS and individual DCX$^+$ cells in tEAE corpus callosum, 2 months p.i. (arrowheads). Scale bars: 50 μm.

(Supplemental Figure 3D). Neuroblast numbers in tEAE mice sacrificed 1 and 2 months p.i. were lower than in controls (Figure 4E). Interestingly, the distribution of migrating cells was also unusual, as they were separated from the ependyma by the astrocytic layer in addition to some small myelinated axons (Figure 4D). Type C cells were more frequent than in the controls. Analysis of cell numbers (Supplemental Table 1) and SVZ composition (Figure 4F) showed that while neuroblasts are the predominant cell type in the controls, tEAE pathology reduced their numbers and increased type C cell proportion, and the B cell increase was only transient (Figure 4F).

Mash1$^+$ SVZ cell pool increases during tEAE due to generation of Olig2$^+$ population. As EM analysis suggested type C cell amplification, we performed immunohistochemical (IHC) quantification on a larger SVZ area using Mash1 as a marker (9). While Mash1$^+$ cell density within the SVZ remained unchanged 3 days p.i., it increased 1.8-fold at 7 days (Figure 5A) and remained significantly higher at 2 weeks and 2 months p.i. compared with control SVZ (1.6-fold). We hypothesized that the Mash1$^+$ cell increase resulted from a generation of a type C cell subpopulation committed to a glial fate. To investigate glial versus neuronal commitment of Mash1$^+$ cells, we examined expression of two transcription factors: Olig2 and Dlx2 (Figure 5). Olig2$^+$ cell density within the SVZ was unchanged at 7 days p.i. but increased 2.45-fold at 2 weeks and 2-fold at 2 months p.i. (Figure 5B). The percentage of Mash1$^+$ cells coexpressing Olig2 also increased 2.37-fold at 2 weeks and 2-fold at 2 months p.i. in tEAE mice compared with the controls, while remaining unchanged at 7 days p.i. (Figure 5, C–I).

In contrast, the density of SVZ Dlx2$^+$ cells decreased 2.5-fold at 7 days, 1.7-fold at 2 weeks, and 1.8-fold at 2 months p.i. (Figure 5J). The percentage of Mash1$^+$ cells labeled for Dlx2 decreased 1.35-fold at 7 days, 1.3-fold at 2 weeks, and 1.45-fold at 2 months p.i. (Figure 5, K–Q).

From these data, we conclude that tEAE increased the total pool of Mash1$^+$ SVZ population. Generation of new Mash1$^+$ cells occurred during the proliferation phase (7 days p.i.), these cells were Dlx2$^-$, and a majority acquired Olig2 expression at later time points.

tEAE decreases OB neurogenesis. Tracing experiments were performed to investigate the consequences of SVZ changes during tEAE on OB neurogenesis. Because this model involves inflammation, a noninvasive tracing consisting of BrdU pulses prior to cytokine injection into immunized animals or sham injection into naive animals was chosen. Preliminary experiments showed that such protocol labeled at least 70% of the Mash1 population. Labeling efficiency in the two experimental groups was comparable, as numbers of SVZ cells that incorporated BrdU did not vary between immunized and naive animals sacrificed immediately following BrdU pulses (Figure 6I). In these animals, positive cells were found in the SVZ/RMS and only occasionally elsewhere in the forebrain. As approximately 2 weeks are required for SVZ neural precursors to become granular neurons (3, 25), mice were sacrificed 2 weeks p.i. Numbers of BrdU$^+$ cells in the OB were decreased by 50% in tEAE compared with sham-treated mice (Figure 6J). Numbers of BrdU$^+$NeuN$^+$ cells within the granule cell layer decreased by 70% (Figure 6, A–F and K), demonstrating impairment of SVZ-derived OB neuronal supply during tEAE. In contrast, numbers of BrdU$^+$Olig2$^+$ cells in tEAE corpus callosum were increased 13-fold (Supplemental Figure 4, B–D). No BrdU-traced GFAP$^+$ cells were detected in the corpus callosum.

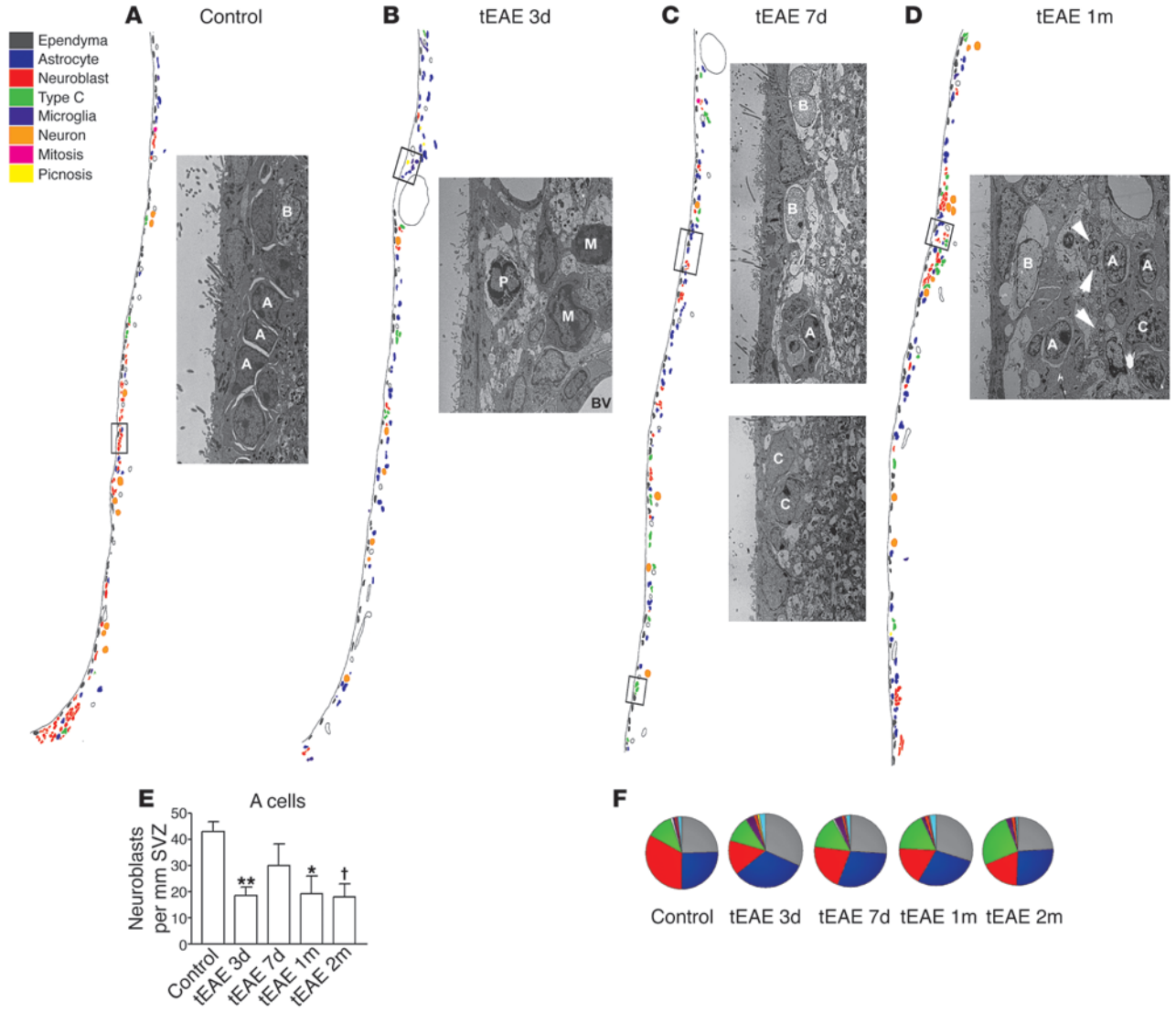

Figure 4

Analysis of SVZ ultrastructure during tEAE. (**A**–**D**) Schematic representation of SVZ organization, with each cell type shown in different color. Neuroblasts are shown in red. Reduction in red cells is obvious at 3 days p.i. in tEAE mice. Some recovery occurs at later time points, but control levels are not reached. Images are illustrations of the boxed areas within each schematic representation. (**A**) Chain of migrating neuroblasts (A) surrounded by astrocytes (B) in the control SVZ. (**B**) Macrophages (M) and pyknotic cell (P) next to blood vessels within tEAE SVZ 3 days p.i. (**C**) Upper panel: Large astrocytes (B) next to small neuroblast chain (A); lower panel: type C cells in tEAE SVZ 7 days p.i. (**D**) Astrocyte (B) processes and small myelinated axons (arrowheads) separate neuroblasts (A) and some C cells (C) from the ependyma in tEAE SVZ 1 month p.i. (**E**) Quantification of A cells in the SVZ of control and tEAE mice. $^{**}P = 0.002$, $^{*}P = 0.01$, $^{\dagger}P = 0.005$ versus control; $n = 3$–4 mice/group; error bars represent SEM. (**F**) SVZ composition represented as average percentages of each cell type within total SVZ cells (3–4 mice/group). While in the control, SVZ neuroblasts (red) predominate, their reduction is obvious during tEAE. The pathology, however, progressively increases type C cells (green). Astrocytes contacting the lateral ventricle are presented in white and non-identified cells in light blue.

BrdU becomes diluted with successive cell divisions. Therefore, to address the long-term effect of tEAE on OB neurogenesis, we quantified DCX$^+$ immature neurons in the OB of tEAE and sham-treated mice. Three months p.i., DCX immunoreactivity in RMS/granule cell layer was significantly decreased in tEAE mice (Figure 6, G, H, and L), demonstrating persistent pathology-induced inhibition of OB neurogenesis.

As BMP signaling via p-SMAD regulates SVZ neurogenesis, and its alteration results in Olig2 upregulation and neuroblast reduction (26), we investigated p-SMAD expression in the SVZ of tEAE mice and controls. In tEAE mice sacrificed 3 months p.i. that showed clear DCX reduction in SVZ and OB, numbers of p-SMAD1/5/8$^+$ SVZ cells were reduced (Figure 7, A–C), suggesting that altered p-SMAD signaling during tEAE may contribute to the sustained neurogenesis impairment.

Targeted EAE impairs long-term olfactory memory. We hypothesized that OB neurogenesis impairment in tEAE could alter olfaction. Experiments were initiated at least 2 weeks p.i. We first established that locomotor activity in tEAE mice was sufficiently preserved to perform olfactory tests (Supplemental Figure 5 and

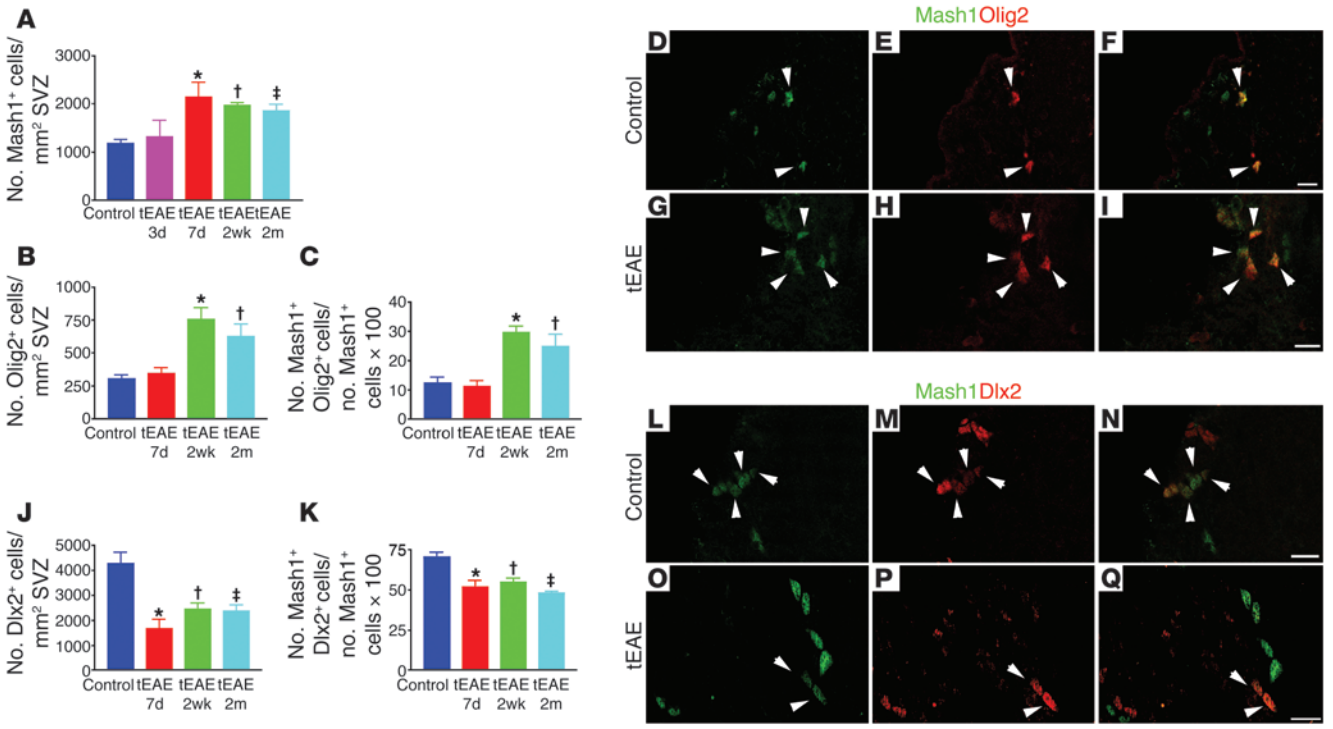

Figure 5

Amplification of Olig2+Mash1+ cell pool and decrease in Dlx2 immunoreactivity in the tEAE SVZ. (**A**) Quantification of Mash1+ SVZ cells (*P = 0.001, †P = 0.0001, ‡P = 0.0003 versus control; n = 5–11 mice/group). (**B**) Quantification of Olig2+ cells in the SVZ (*P = 0.0007, †P = 0.0045 versus control; n = 5–11 mice/group). (**C**) Olig2+ fraction of the Mash1+ cell population in the SVZ increases during tEAE (*P = 0.0001, †P = 0.0182 versus control). (**D**–**I**) Representative images of Mash1 (green) and Olig2 (red) co-immunolabeling in the SVZ of control (**D**–**F**) and tEAE (**G**–**I**) mice at 2 months p.i. (**J**) Quantification of Dlx2+ cells in the SVZ (*P = 0.003, †P = 0.0091, ‡P = 0.0133 versus control; n = 4–7 mice/group). (**K**) Dlx2+ fraction of the Mash1+ cell population in the SVZ diminishes during tEAE (*P = 0.003, †P = 0.0023, ‡P = 0.0002 versus control). (**L**–**Q**) Representative images of Mash1 (green) and Dlx2 (red) co-localization in the SVZ in control (**L**–**N**) and tEAE (**O**–**Q**) mice. Error bars represent SEM. Scale bars: 20 μm.

Supplemental Results). We then examined odorant detection and discrimination, as well as olfactory memory. Odorant discrimination (Figure 8, A and B, and Supplemental Figure 6) and short-term olfactory memory (Figure 8, C and D) were preserved in tEAE mice (see Supplemental Results). Next, we examined long-term olfactory memory. First, water-deprived mice were trained to recognize *n*-amyl acetate as the rewarded stimulus (S^+) and cineole as the non-rewarded stimulus (S^-) using olfactometers (4). Licking water bottle following exposure to S^+ and not licking following S^- were considered as correct decisions, and failure to lick following exposure to S^+ was considered as a "miss" response. Forty days following task consolidation, the ability of mice to recognize S^+ and S^- was retested (Figure 8E). Retention of learned odorants was better in sham than in tEAE mice, as the percentage of correct responses was lower for the latter group (Figure 8F). Memory task error number increased in tEAE mice (Figure 8G) mostly due to miss number (Figure 8H), and these mice performed with higher probability of miss in each S^+ trial, near chance level (Figure 8I). Therefore, we conclude that tEAE impairs long-term olfactory memory.

Altered neurogenesis in the SVZ of MS patients. To assess the relevance of our data in inflammatory demyelinating diseases, we investigated whether neurogenesis was also altered in the SVZ of postmortem MS brains as compared with non-neurological controls. We previously showed a clear expansion of MS SVZ compared with non-neurological controls, based on the increase in cell density, proliferation, and numbers of Sox9+ glial precursors (16). Using the same brain samples and double labeling for GFAPδ to identify SVZ astrocytes/stem cells (27) and MOG to label myelin, we have now observed that the thickness of lateral ventricular wall layer II was increased in the MS compared with control SVZ (Figure 9, A and B). Neurogenesis was investigated by analyzing expression of the specific neuroblast marker DCX in the SVZ of MS patients versus non-neurological cases. Interestingly, DCX-expressing neuroblasts were detected in both MS and control SVZ (Figure 9, C and D), but were rarely observed in the caudate nucleus. Quantification of DCX+ cells in layers I–IV, defined by GFAPδ and MOG co-immunolabeling (Figure 9, A and B), indicated that the DCX+ neuroblast density was significantly reduced in the lateral SVZ of MS brains compared with controls (Figure 9E). Decrease in DCX+ density was present in layers II/III (hypocellular gap and astrocyte ribbon), as well as in layer IV (MOG ribbon).

Discussion

To overcome the difficulty of obtaining forebrain lesions in diffuse EAE and specifically examine SVZ integrity during MS-like pathology, we developed a model of targeted periventricular inflammation/demyelination by modifying a previously described targeting protocol (28). Our model offers several advantages for SVZ studies: (a) inflammatory lesions are found periventricularly in all treated

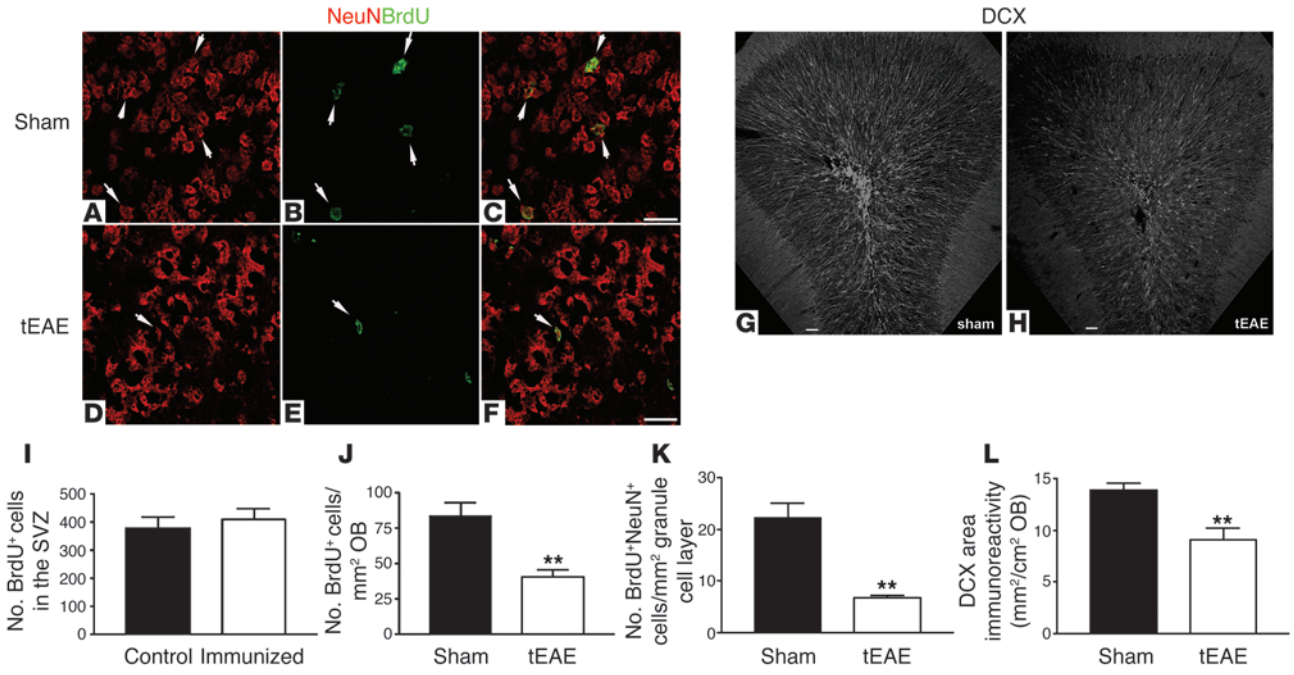

Figure 6

OB neurogenesis decreases during tEAE. Tracing of SVZ progeny was performed by two 2-hour BrdU pulses prior to pathology induction. (**A**–**F**) Representative images of granule cell layer in the OBs of sham-treated (**A**–**C**) and tEAE mice (**D**–**F**) sacrificed 2 weeks following pathology induction and BrdU injections. (**I**) BrdU labeling efficiency of SVZ cells is identical for sham-treated and tEAE mice immediately after the pulse. (**J**) Two weeks p.i., fewer (***P* = 0.0037; *n* = 4–5 mice/group) BrdU$^+$ cells are found in the OB of tEAE compared with sham-treated mice. (**K**) In the granule cell layer, a decrease (***P* = 0.0006; *n* = 4–5 mice/group) in newly formed mature neurons (BrdU$^+$NeuN$^+$) is observed. (**G**, **H**, and **L**) Long-term evaluation of granule cell neurogenesis was performed by quantification of DCX$^+$ immature neurons. (**G** and **H**) Representative images of coronal OB sections labeled with DCX antibody in sham-treated (**G**) and tEAE (**H**) mice sacrificed 3 months p.i. (**L**) Quantification of DCX immunoreactivity (***P* = 0.0029; *n* = 6–7 mice/group). Error bars represent SEM. Scale bars: 20 μm (**A**–**F**), 50 μm (**G** and **H**).

animals, (b) SVZ-proximal demyelination occurs, and (c) cytokine injection represents unequivocally the initiation of the forebrain pathology in all animals, allowing for a precise sequential study of the SVZ dynamics. Examination of SVZ function showed that tEAE inflammation did not hamper pro-oligodendrogenic responses, as it was associated with increased numbers of Olig2-expressing type C cells and SVZ-derived Olig2$^+$ cells in the corpus callosum. However, SVZ neuronal supply to the OB severely diminished and led to a long-term olfactory memory deficit.

Reduction in OB neurogenesis during tEAE appears to result from a combination of distinct events, including survival, migration, and/or differentiation. Neuroblast death occurred during early pathology phases, as evidenced by cleaved caspase-3 labeling and increased numbers of pyknotic features. In addition, emigration of DCX$^+$PSA-NCAM$^+$ cells from the SVZ/RMS was substantial. Possible factors supporting such ectopic migration are chemokine upregulation in the inflamed areas (29, 30), blood vessel changes (31, 32), and modification of astrocyte tunnels (32). Premature/ectopic neuroblast differentiation into mature neurons is unlikely, as tracing studies revealed only occasional BrdU$^+$NeuN$^+$ cells outside the OB (data not shown). Yet an increase in Olig2$^+$Dlx2$^-$ and Olig2$^-$Dlx2$^-$ at the expense of the Dlx2$^+$ proportion of the Mash1$^+$ SVZ population during the pathology suggests type C cell differentiation switch/block as another important contributor to neuroblast reduction. In addition, structural changes within SVZ architecture occur in the areas of early neuroblast loss. These cell-free gaps become occupied by astrocyte processes and myelinated axons, which are most likely inhibitory for reestablishment of normal cell migration toward the OB. We therefore conclude that a combination of early neuroblast death, fate change by type C cells, and structural rearrangements within the SVZ during pathology caused sustained impairment of OB neuronal supply and defective long-term olfactory memory (Figure 7D).

One could argue that neurogenesis impairment could be a direct consequence of cytokine injection, as TNF-α/IFN-γ can modulate NSC behavior (reviewed in ref. 33). Even though cytokine injection into the corpus callosum of naive mice induced a transient increase in inflammatory cell numbers within the SVZ, this treatment was not associated with loss of DCX$^+$PSA-NCAM$^+$ neuroblasts, which was seen only in tEAE mice. Some cytokine-injected, non-immunized mice even showed increased immunoreactivity for DCX, and this is consistent with previous findings indicating that acute inflammation not associated with autoimmune pathology may promote SVZ neurogenesis (34, 35). While it appears clear that in our experiments cytokine injection on its own temporarily changed the SVZ inflammatory status, we found that neurogenesis impairment occurred only when mice were immunized with MOG prior to injection. Possible reasons for this are: (a) the different nature and secretory pattern of infiltrating inflammatory cells in naive and immunized mice, as only in the second case will lymphocytes be primed against brain antigens; and (b) an active immune response in the brain of tEAE mice causing changes in the choroid plexus (36) and consequently altering CSF and therefore the NSCs within the SVZ niche. In conclusion, the ultimate cause of neurogenesis

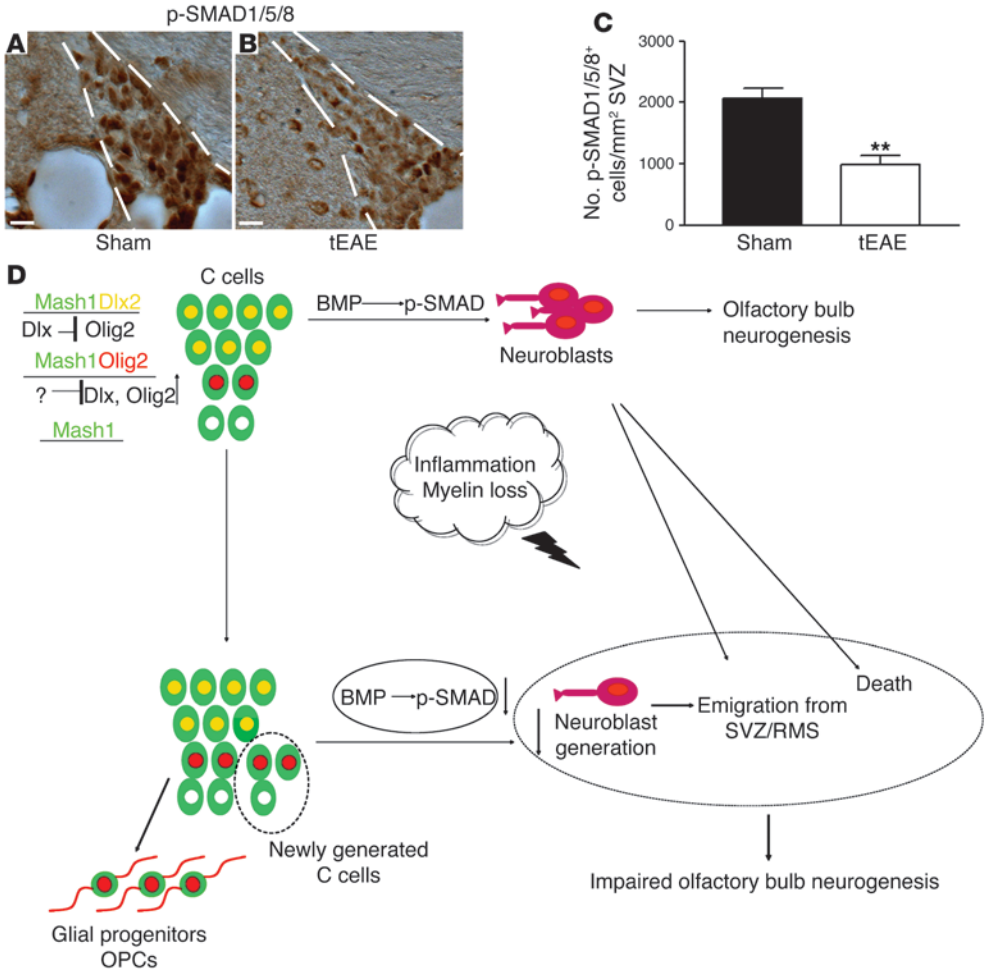

Figure 7

Persistence of tEAE-induced neurogenesis impairment correlates with decreased p-SMAD signaling. (**A** and **B**) IHC for p-SMAD1/5/8 on coronal sections of sham-treated (**A**) and tEAE (**B**) SVZ 3 months p.i. (**C**) Significant decrease in numbers of p-SMAD1/5/8$^+$ SVZ cells in tEAE versus sham-treated mice (**P = 0.0013; n = 5 mice/group). (**D**) Schematic summary of tEAE-induced SVZ changes. In healthy SVZ, 3 type C cell subtypes are detected: the predominant is the Dlx2$^+$ cell (green cells with yellow nucleus) in which Dlx suppresses Olig2 expression. In these cells, BMP signaling through p-SMAD is active, and migrating neuroblasts (violet unipolar cells) are produced. Neuroblasts migrate into the OB and generate new interneurons. The second type C cell subtype is the Olig2$^+$ cell (green cells with red nucleus) in which Dlx2 expression is repressed. These cells are considered as an early source of oligodendrocyte progenitor cells (OPCs; red bipolar cells). A minor percentage of Mash1$^+$ cells is negative for both Dlx2 and Olig2 (green cells with white nucleus). Inflammation induces some neuroblast apoptosis and emigration of others into the inflamed parenchyma. In addition, the pathology amplifies the Mash1$^+$ SVZ population by increasing primarily numbers of Mash1$^+$Olig2$^+$ cells. Decreased p-SMAD signaling during tEAE may contribute to these changes. Moreover, neuroblasts generated still deviate from their default route, possibly due to structural changes within the neurogenic niche and/or attractive cues within the inflamed tissue. The final outcome of such changes is decreased neuronal OB supply. Scale bars: 20 μm.

impairment in tEAE mice appears to be due to complex events associated with active brain inflammation/demyelination as seen in MS, rather than acute injection of proinflammatory stimulus.

Numbers of Olig2$^+$ cells in the SVZ increased during tEAE. While Olig2 labels common neuronal/oligodendrocyte precursors during embryonic development (37), it correlates with oligodendrocyte (6, 8, 9) and astrocyte (8) generation in the postnatal/adult SVZ. It therefore appears that inflammatory demyelination stimulated early glial commitment of SVZ cells, as seen in MS studies (16, 17).

The Olig2$^+$ SVZ cells generated during tEAE were also Mash1$^+$. During tEAE, Mash1$^+$ cell pool amplification occurred during the proliferation phase (7 days p.i.), and these newly generated cells were negative for the neurogenic determinant Dlx2. The absence of Dlx2 in SVZ cells allows for Olig2 upregulation (10), detected at 2 weeks and 2 months p.i. in our model. Mash1 is expressed predominantly by type C cells (9) and by activated type B cells (38), which suggests these as a primary source of SVZ-derived oligodendrocytes during the pathology. These results support previous findings that certain growth factor stimulation induces a pro-oligodendrogenic switch in normal SVZ, with PDGF acting on type B (39) and EGF on type C cells (40). Moreover, amplifying type C cells by EGF treatment following lysolecithin-induced demyelination enhances SVZ oligodendrogenesis (41). Yet it was suggested that neuroblasts can also generate oligodendrocytes (21). While we show that type C is the principal pro-oligodendro-

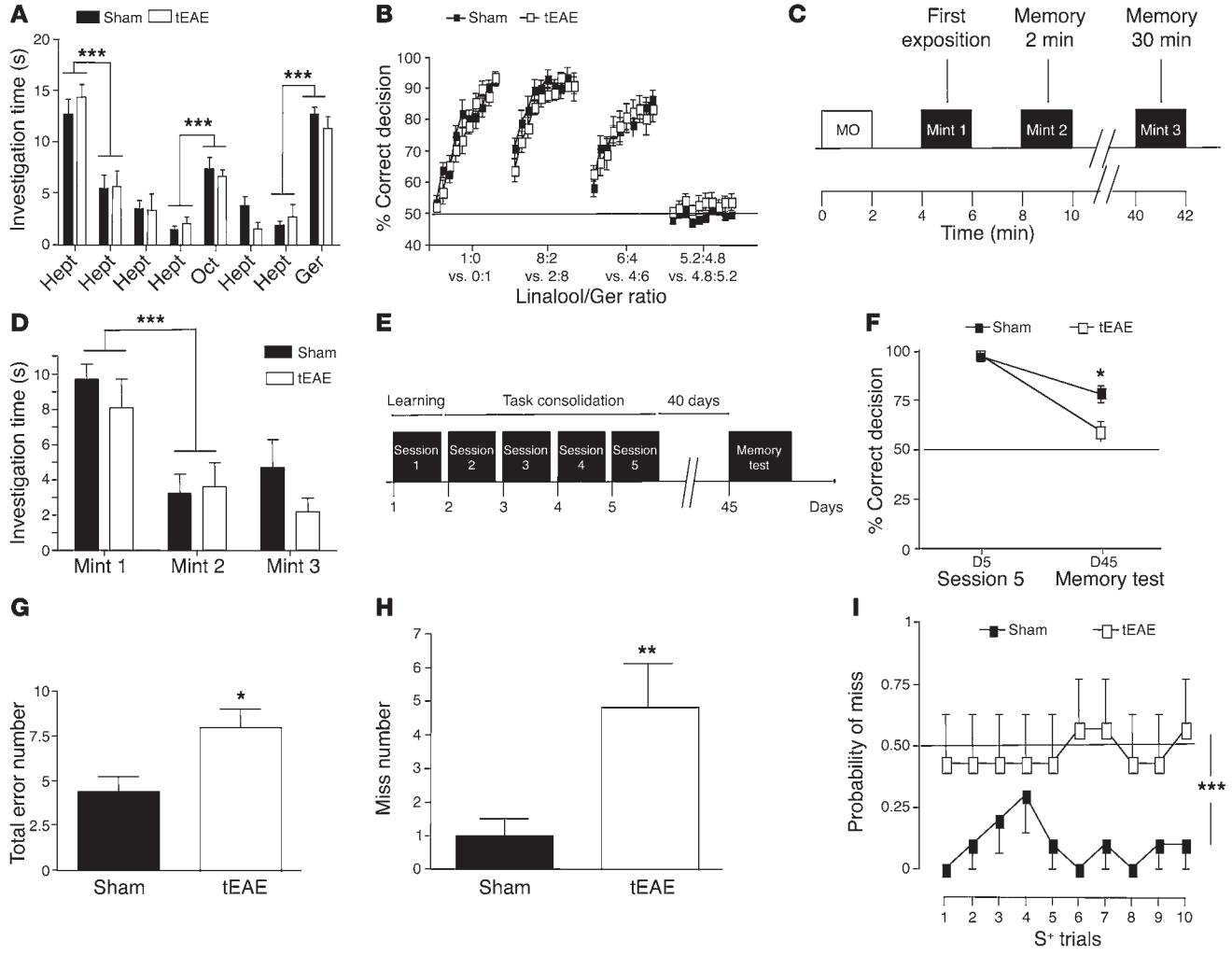

Figure 8

Olfactory dysfunction in tEAE mice. (**A**) Spontaneous olfactory discrimination. Histograms indicate mean time of odorant investigation within 2-minute exposure (rest intervals, 2 minutes). Eight sets of columns represent 4 habituations to heptanal (Hept), dishabituation (similar odorant, octanal [Oct]), 2 habituation recalls (Hept) and a final dishabituation (dissimilar odorant, geraniol [Ger]). ***$P < 0.0001$. (**B**) Reinforced olfactory discrimination between pairs of binary mixtures consisting of different linalool (L, rewarded odorant)/geraniol (no reward) ratios. Vertical axis represents correct response percentage for 10 blocks of 20 trials. Dashed line represents chance level (50%). (**C** and **D**) Short-term olfactory memory was tested by mint odorant presentation twice for 2 minutes (2-minute pause), followed by 30 minutes rest period and then 2-minute memory test (**C**). (**D**) Histograms indicate the mean investigation time. ***$P < 0.0001$. (**E**–**I**) Long-term olfactory memory. (**E**) Mice learned to discriminate (day 1) between 1% *n*-amyl acetate (rewarded odorant, S^+) and 1% cineole (non-rewarded odorant, S^-), which was followed by a 4-day task consolidation (days 2–5) and then a 40-day rest period. Memory was tested in 1 block of 20 trials (10 S^+, 10 S^-, random). (**F**) Mean percentages of correct responses in the training session 5 versus memory test. Chance level is represented by dashed line (50%); *$P = 0.0132$. (**G**) Mean error numbers for memory test: *$P = 0.0151$. (**H**) Mean error numbers in S^+ memory trials: **$P = 0.0067$. (**I**) Mean probability of miss in S^+ trials (error number in S^+ trials/number of S^+ trials): ***$P = 0.0001$. n = 7–9 mice/group. Error bars indicate SEM.

genic SVZ cell during tEAE, we cannot exclude that emigrating neuroblasts in our model (Supplemental Figure 4) may also contribute to oligodendrogenesis.

Neurogenic/gliogenic transcription factor switch by NSCs during tEAE could be triggered by several mechanisms. Those include altered balance of pro-neurogenic versus pro-oligodendrogenic cytokines (42, 43), inflammation-induced redox state modification (44), and previously mentioned PDGF (39) or EGF (40) signaling. Another important regulator of SVZ neurogenesis is BMP signaling via p-SMAD (21, 26), and p-SMAD expression is found on B and C cells, but not on neuroblasts (26). Diminished p-SMAD signaling in the SVZ leads to upregulation of Olig2 expression and reduces neuroblast content (26). Interestingly, reduction in p-SMAD1/5/8^+ cells during tEAE correlated with long-term neurogenesis impairment, thus suggesting that inhibition of BMP signaling contributes to the persistence of SVZ changes. Moreover, BMP signaling inhibition was also reported to induce oligodendrogenesis by type A cells (21).

The effects of EAE inflammation on SVZ have also been a subject of previous studies in mice (22, 23, 45, 46). Importantly, the main similarity among most of these (22, 23, 46) and our study appears to be disturbed neuroblast migration to the OB, which we now show

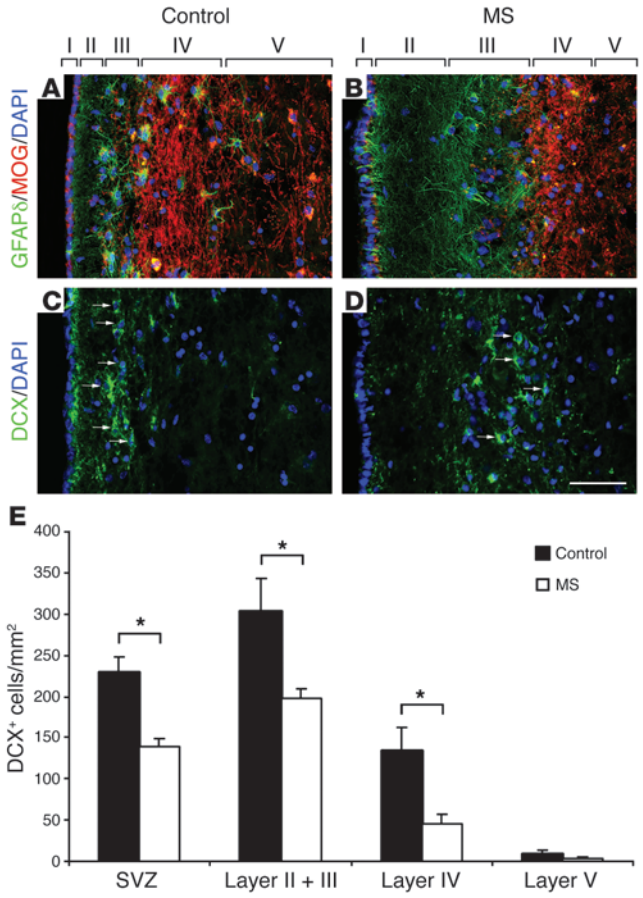

Figure 9
Neurogenesis is decreased in the SVZ of MS brain. Lateral ventricular wall layers I–V were delimited by co-immunolabeling for GFAPδ (green) and MOG (red) in non-neurological control (**A**) and MS brains (**B**). The thickness of layer II is increased in MS compared with non-neurological controls. GFAPδ-expressing cells are mainly detected in layer III (astrocytic ribbon). DCX labeling in non-neurological controls (**C**) and MS SVZ (**D**). (**E**) The number of DCX+ neuroblasts (arrows in **C** and **D**) in the SVZ is significantly decreased in layers II, III, and IV. Error bars indicate SEM. *$P \leq 0.05$. Scale bar: 50 μm.

contributes to impaired OB neurogenesis and long-term olfactory memory. Yet the data regarding SVZ proliferation and oligodendrogenesis appear to differ according to the EAE model used. Whereas in both whole myelin–induced EAE in C57BL/6 mice (22) and proteolipid protein (PLP)–induced relapsing-remitting EAE in Sjl mice (46) SVZ proliferation increased in the acute but not chronic (46) phases, decreased numbers of proliferating SVZ cells at all times were observed in MOG peptide–induced EAE (23). In these previous studies, the criteria for selection of EAE mice for analyses was limb paralysis, which is indicative of spinal cord pathology but not necessarily of the presence of inflammatory demyelinating lesions in the SVZ vicinity. In our study, we correlated SVZ changes specifically to the events within the forebrain. We first observed a decrease in proliferation at 3 days. As the forebrain pathology in all tEAE mice started with cytokine injection, we deduce that the intensity of this initial inflammatory reaction at 3 days p.i. reduces numbers of proliferating SVZ cells by inducing neuroblast death/emigration and somewhat diminishing the C cell proliferation (data not shown). As periventricular inflammation in general EAE models frequently precedes clinical signs (47) that are considered as the initiation of the disease, it could be that the initial SVZ response prior to proliferation during general EAE was missed (22, 46). Our study also shows that at 7 days p.i., very shortly after the initial reduction in numbers of proliferating cells, the niche launches a regenerative attempt. This increase in proliferation is consistent with studies of whole myelin–induced EAE (22) and the acute phase of relapsing-remitting EAE (46) and therefore strengthens the concept of SVZ activation following disease induction. Given that IHC and ultrastructural SVZ analyses showed no difference in numbers of inflammatory cells between 3 days p.i. (proliferation reduction) and 7 days p.i. (proliferation peak), we deduce that the presence of inflammatory cells itself is not sufficient to inhibit SVZ activation. The determining factor may, however, be a different secretory profile of microglial cells at these two time points (42, 43). In chronic phases of tEAE, the SVZ proliferation was not affected, similarly to relapsing-remitting EAE (46), and the main change was oligodendrogenic commitment of C cells, as evidenced by increased expression of Olig2, not detected in other studies (23). This difference may again arise from the fact that occurrence of periventricular demyelination and intensity of inflammation were greatly increased in our model as compared with general MOG-induced EAE. In addition, we show that Olig2 upregulation was due to the commitment of C cells, while others have mostly investigated this phenomenon on neuroblasts (23). One could therefore speculate that MS-like inflammation exerts an inhibitory effect on SVZ neurogenesis and that the presence of proximal demyelinating lesions induces early glial/oligodendrogenic commitment of C cells, also observed in human studies (16, 17).

Previous studies (16, 17) have described increased early gliogenesis in the SVZ of MS patients, suggesting attempts to repair myelin, but the effect of these events on neurogenesis had not been investigated. Interestingly, we now find that as in tEAE mice, lateral SVZ from MS patients showed decreased neuroblast content. It therefore appears that following inflammatory attacks and myelin loss in proximal areas, neurogenesis/gliogenesis balance by human SVZ precursors becomes altered, leading to increased attempts at glial production. Independent of the success of such attempts in generating oligodendrocytes, this early switch appears to be detrimental for neuroblast generation.

Inflammation-triggered decreases in OB neuronal supply during tEAE significantly altered long-term olfactory memory, but not short-term olfactory memory or odorant discrimination, supporting previous findings that long-term olfactory memory is the main function of adult SVZ neurogenesis (4, 5). Unaffected olfactory memory following OB neurogenesis ablation has also been reported (48, 49), but these studies employed nonoperant tasks to examine olfaction, while we and others reporting a decrease in olfactory memory (4, 5) have employed operant tasks. These two types of tests may actually be examining different olfactory functions (50).

One could argue that olfactory deficit during tEAE is due to events other than SVZ neurogenesis impairment. No decrease in hippocampal immunoreactivity for DCX in tEAE mice was detected (data not shown), excluding the role of hippocampal impairment in memory deficit. Moreover, apoptotic neurons in tEAE cortex were not observed. Although we cannot exclude that forebrain inflammation may specifically affect functioning of olfactory areas involved in memory, the fact that similar func-

tional deficits occur following non-inflammatory SVZ neurogenesis impairment (4, 5) strongly suggests that long-term olfactory memory deficit in tEAE mice is a direct consequence of decreased neuronal supply to the OB.

Interestingly, olfactory dysfunction occurs during MS (51) and is characterized by defective odor identification, although odor the detection threshold appears preserved (18), as seen in tEAE mice. So far, defective olfaction during MS has been attributed to inflammatory lesion load within frontal/temporal regions (18, 52), although relative olfactory tract sparing has been reported previously (18). Our results suggest that inflammation-induced SVZ changes may provide an alternative/complementary explanation for MS olfactory deficits and support the growing idea that adult NSC dysfunction contributes to pathogenesis in brain disorders (53). Further insights into the functional role of human SVZ neurogenesis are, however, required to ultimately support the validity of this proof of concept in the clinical scenario.

Methods

Targeted EAE induction

Nine- to 10-week-old female C57BL/6 mice were purchased from Janvier. Experiments were performed under French Agricultural Ministry–Animal Welfare licence number B75-13-08. Mice were housed under standard conditions and were given ad libitum access to dry food and water. Subclinical immunization was performed by subcutaneous injection of 25 μg MOG peptide (MOG_{35-55}, NeoMPS) in CFA (Difco). Sixteen to 20 days later, mice were anesthetized with Imalgene/xylazine. Two microliters of a cocktail containing 250 ng mouse TNF-α (R&D) and 1,500 U IFN-γ (Sigma-Aldrich) in saline was stereotaxically injected into the corpus callosum using the following coordinates: antero-posterior 1.5, lateral 1, deep 2.1. Sham controls were saline injected, and cytokine injection controls were non-immunized animals injected with cytokine cocktail. Immunization controls were immunized noninjected mice.

Perfusion and tissue processing

Mice were euthanized with Imalgene and perfused with a 2% or 4% PFA (Sigma-Aldrich) solution in PBS for IHC analysis or Karnovsky fixative (2% PFA/2.5% glutaraldehyde [Electron Microscopy Sciences] in 0.1 M phosphate buffer [PB]) for EM. For IHC analysis, brains were placed in 20% sucrose solution and frozen in embedding medium (Thermo Electron). Twelve-microgram sagittal or coronal sections were cut. In experiments evaluating DCX immunoreactivity in the OB, brains were post-fixed overnight in 4% PFA and 40-μm-thick vibratome sections cut.

For EM analyses, brains were post-fixed overnight and washed in 0.1 M PB, and 200-μm-thick coronal vibratome sections were cut. The next day, the tissue was post-fixed in 2% osmium for 2 hours, rinsed, dehydrated, and embedded in Araldite epoxy resin (Fluka).

Ultrastructural analysis of the SVZ

To study the overall SVZ organization, 1.5-μm semi-thin sections were cut with a diamond knife and stained with 1% toluidine blue. Ultrathin (70-nm) sections were cut, stained with lead citrate, and examined under a transmission electron microscope (Tecnai Spirit G2, FEI) using a digital camera (Morada). The number of profiles corresponding to different cell types along the ventricular wall was determined. Different cell types in the adult SVZ were identified as described previously (24) and scored as cell number/mm SVZ length or the percentage of each cell type over the total number of cells counted.

Antibodies and IHC

Primary antibodies used were: anti–PSA-NCAM, mouse anti-GFAP, anti-BrdU, and anti-CD19 (Abcys); anti-DCX (Abcam), anti-Mash1, and anti–Ki-67 (BD Biosciences — Pharmingen); anti–cleaved caspase-3 and anti–p-Smad1/5/8 (Cell Signaling Technology); anti-Olig2, anti-MBP, anti-NeuN, and anti-GFAPδ (Millipore); anti-Dlx2 (54); anti-MOG (hybridoma supernatant, provided by C. Linnington, University of Glasgow, Glasgow, United Kingdom); anti-CD45, anti-CD8, and anti-CD4 (Invitrogen); NF-200 (Sigma-Aldrich); rabbit anti-GFAP (Dako); and anti-F4/80 (Serotec). Secondary antibodies included antibodies from Jackson ImmunoResearch Europe and Alexa Fluor–conjugated antibodies (Invitrogen).

Sections were air dried for 1 hour and rehydrated in PBS. For IHC of transcription factors (Mash1, Olig2, and Dlx2), antigen retrieval was performed by microwaving the sections in a retrieval buffer (Vector Laboratories/Dako) for 2 minutes. After washing, appropriate blocking buffer was applied for 30 minutes, followed by primary antibody incubation overnight at 4°C. Sections were washed and secondary antibodies applied for 1 hour. For p-Smad1/5/8 IHC, the signal was amplified using biotinylated secondary antibody followed by horseradish peroxidase–conjugated streptavidin (Invitrogen) and revealed using a DAB kit (Abcys) or by Alexa Fluor–conjugated streptavidin (Invitrogen) for fluorescence microscopy. Nuclei were counterstained with Hoechst.

Quantification of different cell types within the SVZ/OB

Images were taken from 4 consecutive SVZ sections separated by 144 μm at ×40 magnification using a digital camera (SPOT Flex, SPOT Imaging Solutions) attached to a microscope (Leica) and imported into NIH ImageJ software (http://rsb.info.nih.gov/ij/). Three to 5 images/section were taken to cover the entire SVZ length. The SVZ was delimited on the DAPI channel and imported onto red/green channels to regionally restrict the analysis. For each image, the SVZ area was measured and positive cells were counted. Results are presented as the total number of positive cells per SVZ area measured. Colocalization studies were performed strictly using nuclear markers by evaluating numbers of cells labeled at both red and green channels.

Quantification of PSA-NCAM or DCX in SVZ/OB was performed by measuring their immunoreactivity within the surface area examined. The SVZ/OB area was delimited on the DAPI channel and transferred onto the channel corresponding to the antigen of interest. The threshold was established and percentage of area labeled within the total area examined measured. Results are presented as mm^2 surface labeled/cm^2 total surface.

Quantification of DCX^+ cells in MS and control SVZ was performed on digital images (ImageJ software) of 3 serial sections (100 μm apart). Because the human SVZ is heterogeneous in size and composition, we restricted our study to the lateral SVZ facing the caudate nucleus and dorsal to the striatal vein as previously described (16). Data are expressed as the mean number of cells ± SEM per surface SVZ.

Proliferation and tracing assays

Mice were injected intraperitoneally with 100 μl of 10 mg/ml BrdU solution in sterile saline 2 times with a 2-hour interval. For evaluation of SVZ proliferation, mice were sacrificed 2 hours following the second pulse. For tracing experiments, mice were sacrificed 2 weeks following BrdU pulses. BrdU IHC was performed as previously described (22).

Olfaction study

For olfaction experiments, tEAE and sham-injected mice were injected bilaterally. Animals were tested in Pasteur Institute animal care facilities officially registered for experimental studies on rodents (French Agricultural Ministry–Animal Welfare approval number for animal care facilities, A75-15-08; 75-585 for animal experimentation).

Olfactory discrimination. For the olfactory discrimination task, we used a habituation-dishabituation test (4). No conditioning or deprivation was performed before the tasks. Test cages were composed of boxes with two compartments separated by an aluminum partition (diameter of holes, 0.5 cm). A filter paper (Whatman), impregnated with 10 μl mineral oil (Sigma-Aldrich) containing 0.4% odorant solution, was introduced in the lower compartment. Mice were trained with 6 exposures to linalool (session 1). They were then exposed to odorants as follows (sessions 2–4, 2-minute exposure): 4 exposures to the first odorant (habituation); 1 exposure to a similar odorant; 2 exposures to the habituation odorant; 1 exposure to a dissimilar odorant (dishabituation). A 2-minute interval was left between each trial. We measured the time mice spent investigating each odorant. Odorant recognition was defined by a decrease in investigation time compared with previous presentation of the same odorant.

Short-term olfactory memory. One day after the last habituation-dishabituation session, mice were exposed to mint odorant twice for 5 minutes with a 2-minute interval pause and then reexposed to mint following a 30-minute resting period. Odorant investigation time was recorded.

Rewarded olfactory discrimination. Odorant detection threshold: Mice were maintained on a 1-ml/d water deprivation diet for 7 days. They were then trained using olfactometers (4) to respond to the presence of linalool diluted in mineral oil (S^+) by licking the water delivery tube situated out of the odorant sampling port (5-cm distance) and to refrain from responding to the presence of mineral oil (negative stimulus, S^-). A licking response following an S^+ trial and no licking following an S^- trial were scored as correct hit and correct rejection, respectively. A 5-μl droplet of water was given as a reward following a hit. A licking response following an S^- trial and no licking following an S^+ trial were scored as errors: false alarm and miss, respectively. The ability of mice to detect successively descending concentrations of linalool diluted in mineral oil was tested daily in 10 blocks of 20 trials. Accuracy (percentage of correct responses) was scored for each block ([hits + correct rejections]/20 × 100).

Odorant mixture discrimination: Mice were trained to distinguish 1% linalool (L) from geraniol (G) for 10 blocks of 20 trials (task 1). Then they were given 10 blocks of 20 trials for each of the following 2-odorant mixture tasks: task 2: S^+ was 0.8% L + 0.2% G and S^- was 0.2% L + 0.8% G; task 3: S^+ was 0.6% L + 0.4% G and S^- was 0.4% L + 0.6% G; task 5: S^+ was 0.52% L+ 0.48% G and S^- was 0.48% L + 0.52% G.

Long-term memory test. Mice were maintained on a 1-ml/day water deprivation diet for 7 days and then given 5 daily training sessions of 10 blocks of 20 trials for a 2-odorant rewarded task (S^+ was 1% *n*-amyl acetate; S^- was 1% cineole). Mice were then left in their cages for 40 days and subjected to partial water deprivation for the 7 last days. No water was given on day 39; the following day, mice were subjected to a 20-trial memory test (2-odorant task).

MS tissue samples

Postmortem MS brain samples and control brain samples from patients who had died from non-neurological disease were obtained from the UK Multiple Sclerosis Tissue Bank (R. Reynolds, Imperial College, London, United Kingdom). Three MS cases with well-characterized periventricular and striatal lesions (16) were used in this study, including secondary progressive (SP, 2 cases) and relapsing progressive (RP, 1 case). For these MS cases, the average duration of the disease since the onset of the first symptoms was 18.33 years (range, 8–31). The mean age was 51 years (range, 38–69) for MS cases and 92.5 (range, 90–98) years for controls. The death tissue preservation delay varied between 7 and 19 hours (Supplemental Table 2). Histological assessment of MS lesions was performed using Luxol fast blue/cresyl violet and oil red O (macrophages filled with myelin debris) staining, and lesion activity was determined as previously described (16).

Statistics

All data are expressed as mean ± SEM. Statistical analyses were carried out using Prism software (GraphPad Software), with P values less than 0.05 considered significant. For IHC and EM analyses, data were analyzed using parametric statistics, with 1-way ANOVA followed by unpaired 2-tailed Student's t test. Behavioral data were analyzed using 2-way ANOVA for repeated measures, followed by unpaired 2-tailed Student's t test. Statistical analyses relevant to data are presented in the figure legends.

Study approval

The animal studies described in this work were performed under French Agricultural Ministry–Animal Welfare licence numbers B75-13-08 and A75-585. Concerning the use of human material, tissues were collected with the donors' fully informed consent via a prospective donor scheme following ethical approval by the London Multicenter Research Ethics Committee (MREC 02/2/39).

Acknowledgments

We would like to acknowledge technical assistance of Mario Soriano (J.M. Garcia-Verdugo's laboratory), Dominique Langui (Imaging Platform, CRICM), and Cyrille Deboux (A. Baron-Van Evercooren's laboratory). We particularly thank Magdalena Götz for valuable suggestions regarding the role of the BMP pathway in regulating SVZ neurogenesis/gliogenesis and Richard Reynolds for providing human tissue for analyses. In addition, we thank Danielle Pham-Dinh, Bill Blakemore, and Carlos Belmonte for discussions. This work was supported by INSERM, the European Leukodystrophy Association (ELA), Ecole des Neurosciences de Paris (ENP), French Society for Multiple Sclerosis (ARSEP), Spanish Ministry of Science and Innovation, Instituto de Salud Carlos III, Red de Terapia Celular, Consellería de Educación (PROMETEO), and the life insurance company Aprionis. V. Tepavcevic was supported by UPMC, Fondation pour la Recherche Médicale (FRM), Novartis, and COST Action MYELINET BM0604 and NEURINFNET BM0603. B. Nait-Oumesmar and A. Baron-Van Evercooren are recipients of a Contrat d'Interface AP-HP (Fédération de Neurologie, Hôpital Pitié-Salpêtrière, Paris).

Received for publication May 27, 2011, and accepted in revised form September 21, 2011.

Address correspondence to: Anne Baron-Van Evercooren, INSERM UMR-S 975, CHU Pitié-Salpêtrière, 47 Boulevard de l'Hôpital, Paris 75013, France. Phone: 33.1.57174123; Fax: 33.1.57274788; E-mail: anne.baron@upmc.fr.

1. Alvarez-Buylla A, Lim D. For the long run: maintaining germinal niches in the adult brain. *Neuron*. 2004;41(5):683–686.
2. Doetsch F, Caillé I, Lim D, García-Verdugo J, Alvarez-Buylla A. Subventricular zone astrocytes are neural stem cells in the adult mammalian brain. *Cell*. 1999;97(6):703–716.
3. Carleton A, Petreanu L, Lansford R, Alvarez-Buylla A, Lledo P. Becoming a new neuron in the adult olfactory bulb. *Nat Neurosci*. 2003;6(5):507–518.
4. Lazarini F, et al. Cellular and behavioral effects of cranial irradiation of the subventricular zone in adult mice. *PLoS One*. 2009;4(9):e7017.
5. Sultan S, Mandairon N, Kermen F, Garcia S, Sacquet J, Didier A. Learning-dependent neurogenesis in the olfactory bulb determines long-term olfactory memory. *FASEB J*. 2010;24(7):2355–2363.
6. Menn B, Garcia-Verdugo J, Yaschine C, Gonzalez-Perez O, Rowitch D, Alvarez-Buylla A. Origin of oligodendrocytes in the subventricular zone of the adult brain. *J Neurosci*. 2006;26(30):7907–7918.
7. Hack M, et al. Neuronal fate determinants of adult olfactory bulb neurogenesis. *Nat Neurosci*. 2005;8(7):865–872.

8. Marshall C, Novitch B, Goldman J. Olig2 directs astrocyte and oligodendrocyte formation in postnatal subventricular zone cells. *J Neurosci*. 2005; 25(32):7289–7298.
9. Parras C, Hunt C, Sugimori M, Nakafuku M, Rowitch D, Guillemot F. The proneural gene Mash1 specifies an early population of telencephalic oligodendrocytes. *J Neurosci*. 2007;27(16):4233–4242.
10. Petryniak M, Potter G, Rowitch D, Rubenstein J. Dlx1 and Dlx2 control neuronal versus oligodendroglial cell fate acquisition in the developing forebrain. *Neuron*. 2007;55(3):417–433.
11. Sanai N, et al. Unique astrocyte ribbon in adult human brain contains neural stem cells but lacks chain migration. *Nature*. 2004;427(6976):740–744.
12. Curtis M, et al. Human neuroblasts migrate to the olfactory bulb via a lateral ventricular extension. *Science*. 2007;315(5816):1243–1249.
13. Bédard A, Parent A. Evidence of newly generated neurons in the human olfactory bulb. *Brain Res Dev Brain Res*. 2004;151(1–2):159–168.
14. Franklin R, Ffrench-Constant C. Remyelination in the CNS: from biology to therapy. *Nat Rev Neurosci*. 2008;9(11):839–855.
15. Patrikios P, et al. Remyelination is extensive in a subset of multiple sclerosis patients. *Brain*. 2006; 129(pt 12):3165–3172.
16. Nait-Oumesmar B, et al. Activation of the subventricular zone in multiple sclerosis: evidence for early glial progenitors. *Proc Natl Acad Sci U S A*. 2007; 104(11):4694–4699.
17. Wu C, et al. Beta4 tubulin identifies a primitive cell source for oligodendrocytes in the mammalian brain. *J Neurosci*. 2009;29(24):7649–7657.
18. Demarquay G, Ryvlin P, Royet JP. Olfaction and neurological diseases: a review of the literature [in French]. *Rev Neurol (Paris)*. 2007;163(2):155–167.
19. Nait-Oumesmar B, Decker L, Lachapelle F, Avellana-Adalid V, Bachelin C, Van Evercooren A. Progenitor cells of the adult mouse subventricular zone proliferate, migrate and differentiate into oligodendrocytes after demyelination. *Eur J Neurosci*. 1999;11(12):4357–4366.
20. Aguirre A, Dupree J, Mangin J, Gallo V. A functional role for EGFR signaling in myelination and remyelination. *Nat Neurosci*. 2007;10(8):990–1002.
21. Jablonska B, et al. Chordin-induced lineage plasticity of adult SVZ neuroblasts after demyelination. *Nat Neurosci*. 2010;13(5):541–550.
22. Picard-Riera N, et al. Experimental autoimmune encephalomyelitis mobilizes neural progenitors from the subventricular zone to undergo oligodendrogenesis in adult mice. *Proc Natl Acad Sci U S A*. 2002;99(20):13211–13216.
23. Pluchino S, et al. Persistent inflammation alters the function of the endogenous brain stem cell compartment. *Brain*. 2008;131(pt 10):2564–2578.
24. Doetsch F, García-Verdugo J, Alvarez-Buylla A. Cellular composition and three-dimensional organization of the subventricular germinal zone in the adult mammalian brain. *J Neurosci*. 1997; 17(13):5046–5061.
25. Petreanu L, Alvarez-Buylla A. Maturation and death of adult-born olfactory bulb granule neurons: role of olfaction. *J Neurosci*. 2002;22(14):6106–6113.
26. Colak D, et al. Adult neurogenesis requires Smad4-mediated bone morphogenic protein signaling in stem cells. *J Neurosci*. 2008;28(2):434–446.
27. Roelofs RF, et al. Adult human subventricular, subgranular, and subpial zones contain astrocytes with a specialized intermediate filament cytoskeleton. *Glia*. 2005;52(4):289–300.
28. Kerschensteiner M, et al. Targeting experimental autoimmune encephalomyelitis lesions to a predetermined axonal tract system allows for refined behavioral testing in an animal model of multiple sclerosis. *Am J Pathol*. 2004;164(4):1455–1469.
29. Robin A, et al. Stromal cell-derived factor 1alpha mediates neural progenitor cell motility after focal cerebral ischemia. *J Cereb Blood Flow Metab*. 2006; 26(1):125–134.
30. Yan Y, Sailor K, Lang B, Park S, Vemuganti R, Dempsey R. Monocyte chemoattractant protein-1 plays a critical role in neuroblast migration after focal cerebral ischemia. *J Cereb Blood Flow Metab*. 2007; 27(6):1213–1224.
31. Thored P, Wood J, Arvidsson A, Cammenga J, Kokaia Z, Lindvall O. Long-term neuroblast migration along blood vessels in an area with transient angiogenesis and increased vascularization after stroke. *Stroke*. 2007;38(11):3032–3039.
32. Whitman M, Fan W, Rela L, Rodriguez-Gil D, Greer C. Blood vessels form a migratory scaffold in the rostral migratory stream. *J Comp Neurol*. 2009; 516(2):94–104.
33. Gonzalez-Perez O, Jauregui-Huerta F, Galvez-Contreras AY. Immune system modulates the function of adult neural stem cells. *Curr Immunol Rev*. 2010;6(3):167–173.
34. Guerra-Crespo M, et al. Transforming growth factor-alpha induces neurogenesis and behavioral improvement in a chronic stroke model. *Neuroscience*. 2009;160(2):470–483.
35. Ekdahl CT, Kokaia Z, Lindvall O. Brain inflammation and adult neurogenesis: the dual role of microglia. *Neuroscience*. 2009;158(3):1021–1029.
36. Strazielle N, Ghersi-Egea JF. Choroid plexus in the central nervous system: biology and physiopathology. *J Neuropathol Exp Neurol*. 2000;59(7):561–574.
37. Rowitch D. Glial specification in the vertebrate neural tube. *Nat Rev Neurosci*. 2004;5(5):409–419.
38. Pastrana E, Cheng L, Doetsch F. Simultaneous prospective purification of adult subventricular zone neural stem cells and their progeny. *Proc Natl Acad Sci U S A*. 2009;106(15):6387–6392.
39. Jackson E, et al. PDGFR alpha-positive B cells are neural stem cells in the adult SVZ that form glioma-like growths in response to increased PDGF signaling. *Neuron*. 2006;51(2):187–199.
40. Doetsch F, Petreanu L, Caille I, Garcia-Verdugo J, Alvarez-Buylla A. EGF converts transit-amplifying neurogenic precursors in the adult brain into multipotent stem cells. *Neuron*. 2002; 36(6):1021–1034.
41. Gonzalez-Perez O, Romero-Rodriguez R, Soriano-Navarro M, Garcia-Verdugo J, Alvarez-Buylla A. Epidermal growth factor induces the progeny of subventricular zone type B cells to migrate and differentiate into oligodendrocytes. *Stem Cells*. 2009; 27(8):2032–2043.
42. Butovsky O, et al. Induction and blockage of oligodendrogenesis by differently activated microglia in an animal model of multiple sclerosis. *J Clin Invest*. 2006;116(4):905–915.
43. Butovsky O, et al. Microglia activated by IL-4 or IFN-gamma differentially induce neurogenesis and oligodendrogenesis from adult stem/progenitor cells. *Mol Cell Neurosci*. 2006;31(1):149–160.
44. Prozorovski T, et al. Sirt1 contributes critically to the redox-dependent fate of neural progenitors. *Nat Cell Biol*. 2008;10(4):385–394.
45. Muzio L, et al. Cxcl10 enhances blood cells migration in the sub-ventricular zone of mice affected by experimental autoimmune encephalomyelitis. *Mol Cell Neurosci*. 2010;43(3):268–280.
46. Rasmussen S, et al. Reversible neural stem cell niche dysfunction in a model of multiple sclerosis. *Ann Neurol*. 2011;69(5):878–891.
47. Brown DA, Sawchenko PE. Time course and distribution of inflammatory and neurodegenerative events suggest structural bases for the pathogenesis of experimental autoimmune encephalomyelitis. *J Comp Neurol*. 2007;502(2):236–260.
48. Imayoshi I, et al. Roles of continuous neurogenesis in the structural and functional integrity of the adult forebrain. *Nat Neurosci*. 2008; 11(10):1153–1161.
49. Breton-Provencher V, Lemasson M, Peralta MR 3rd, Saghatelyan A. Interneurons produced in adulthood are required for the normal functioning of the olfactory bulb network and for the execution of selected olfactory behaviors. *J Neurosci*. 2009; 29(48):15245–15257.
50. Linster C, Johnson B, Morse A, Yue E, Leon M. Spontaneous versus reinforced olfactory discriminations. *J Neurosci*. 2002;22(16):6842–6845.
51. Zivadinov R, Zorzon M, Monti Bragadin L, Pagliaro G, Cazzato G. Olfactory loss in multiple sclerosis. *J Neurol Sci*. 1999;168(2):127–130.
52. Doty R, Li C, Mannon L, Yousem D. Olfactory dysfunction in multiple sclerosis: relation to longitudinal changes in plaque numbers in central olfactory structures. *Neurology*. 1999;53(4):880–882.
53. Taupin P. Adult neurogenesis, neuroinflammation and therapeutic potential of adult neural stem cells. *Int J Med Sci*. 2008;5(3):127–132.
54. Kuwajima T, Nishimura I, Yoshikawa K. Necdin promotes GABAergic neuron differentiation in cooperation with Dlx homeodomain proteins. *J Neurosci*. 2006;26(20):5383–5392.